

# Star Formation in the Outer Galaxy: Coronal Properties of NGC 1893<sup>★</sup>

M. Caramazza<sup>1</sup>, G. Micela<sup>1</sup>, L. Prisinzano<sup>1</sup>, S. Sciortino<sup>1</sup>, F. Damiani<sup>1</sup>, F. Favata<sup>2</sup>, J. R. Stauffer<sup>3</sup>, A. Vallenari<sup>4</sup>, and S. J. Wolk<sup>5</sup>

<sup>1</sup> INAF Osservatorio Astronomico di Palermo, Piazza del Parlamento 1, 90134 Palermo, Italy

<sup>2</sup> European Space Agency, 8-10 rue Mario Nikis, 75015 Paris, France

<sup>3</sup> Spitzer Science Center, Caltech 314-6, Pasadena, CA 91125, USA

<sup>4</sup> INAF, Osservatorio Astronomico di Padova, Vicoletto dell'Osservatorio 5, 35122 Padova, Italy

<sup>5</sup> Harvard-Smithsonian Center for Astrophysics, 60 Garden Street, Cambridge, MA 02138, USA

email:mcarama@astropa.unipa.it

Received ; accepted

## ABSTRACT

**Context.** The outer Galaxy, where the environmental conditions are different from the solar neighbourhood is a laboratory in which it is possible to investigate the dependence of star formation process on the environmental parameters.

**Aims.** We investigate the X-ray properties of NGC 1893, a young cluster ( $\sim 1-2$  Myr) in the outer part of the Galaxy ( galactic radius  $\geq 11$  kpc) where we expect differences in the disk evolution and in the mass distribution of the stars, to explore the X-ray emission of its members and compare it with that of young stars in star forming regions near to the Sun.

**Methods.** We analyze 5 deep *Chandra* ACIS-I observations with a total exposure time of 450 ks. Source events of the 1021 X-ray sources have been extracted with the IDL-based routine ACIS-Extract. Using spectral fitting and quantile analysis of X-ray spectra, we derive X-ray luminosities and compare the respective properties of Class II and Class III members. We also evaluate the variability of sources using the Kolmogorov-Smirnov test and we identify flares in the lightcurves.

**Results.** The X-ray luminosity of NGC 1893 X-ray members is in the range  $10^{29.5} - 10^{31.5}$  erg s<sup>-1</sup>. Diskless stars are brighter in X-rays than disk-bearing stars, given the same bolometric luminosity. We found that 34% of the 1021 lightcurves appear variable and that they show 0.16 flare per source, on average. Comparing our results with those relative to the Orion Nebula Cluster, we find that, accounting for observational biases, the X-ray properties of NGC 1893 and the Orion ones are very similar.

**Conclusions.** The X-ray properties in NGC 1893 are not affected by the environment and the stellar population in the outer Galaxy may have the same coronal properties of nearby star forming regions. The X-ray luminosity properties and the X-ray luminosity function appear to be universal and can therefore be used for distance estimations and for determining stellar properties as already suggested by Feigelson and collaborators.

**Key words.** Stars: coronae, pre-main sequence, luminosity function, open clusters and associations: individual : NGC 1893, X-rays: stars

## 1. Introduction

The formation of stars, the evolution of circumstellar disks and eventually the formation of planets are key research topics in modern astrophysics. So far, several star forming regions of different ages and in different environment conditions have been studied in order to explore the parameter space as well as possible. Although several questions have been answered, some aspects of the star formation mechanism and initial stellar evolution are still obscure.

A key question is whether and how star formation depends on the environmental conditions. Since the Jeans mass depends on gas temperature, chemical abundances, and density (cf. Elmegreen, 2002, 2004), some dependencies on the physical conditions of star-forming clouds are expected. Moreover, the observed variation in the initial mass function (IMF) at low stellar masses across different environments (Reylé & Robin, 2001; Gould et al., 1998) suggests that gravity is not the only important

parameter in the cloud fragmentation and subsequent evolution. As a consequence, other processes, e.g. turbulence and/or magnetic field strength in the cloud have been considered (Shu et al., 1987; Padoa & Nordlund, 1999; Mac Low & Klessen, 2004).

In this context, a natural way to explore the differences due to the environment is to look at the outer Galaxy. Molecular clouds and very young stellar associations are present also at large distances from the Galactic Center (Snell et al., 2002), implying that star formation is occurring in these regions. Conditions in the outer Milky Way are thought to be less favorable to star formation, when compared with those in the solar neighborhood: the average surface and volume densities of atomic and molecular hydrogen are much smaller than in the solar neighborhood or in the inner Galaxy (Wouterloot et al., 1990), the interstellar radiation field is weaker (Mathis et al., 1983), prominent spiral arms are lacking and there are fewer supernovae to act as external triggers of star formation. Metal content is, on average, smaller (Wilson & Matteucci, 1992), decreasing radiative cooling and therefore increasing cloud temperatures and consequently pressure support. Moreover, the pressure of the inter-cloud medium in the outer Galaxy is smaller (Elmegreen, 1989).

<sup>★</sup> Tables 1 and 3 are only available in electronic form at the CDS via anonymous ftp to cdsarc.u-strasbg.fr (130.79.128.5) or via <http://cdsweb.u-strasbg.fr/cgi-bin/qcat?J/A+A/>

Given these relevant differences, the study of star forming regions in the outer Galaxy is likely to be helpful to ascertain the role of environmental conditions in the star formation process. First of all, the environmental conditions could affect the evolution of protoplanetary disks: Yasui et al. (2009) measured, in the extreme outer Galaxy, a disk frequency significantly lower than in the inner part of the Milky Way. The eventual dependence of disk lifetimes on metallicity could affect the formation of planets and may give also insight into the “planet-metallicity correlation”, since stars known to harbor giant planets appear to preferentially be metal rich (Santos et al., 2003; Fischer & Valenti, 2005, and references therein). Moreover, a recent theoretical works (Ercolano & Clarke, 2009) shows that the disk lifetime in regions of different metallicity can give insight into the general mechanism of disk dispersal, allowing to discriminate between the two currently dominant models of disk dispersal: photoevaporation and planet formation.

In principle, the metal abundance differences between the inner and the outer Galaxy could also affect the coronal properties. Indeed, the thickness of the outer convection zone in low mass stars is a function of metallicity (Pizzolato et al., 2001). This, in turn, likely changes the dynamo process itself, i.e. the X-ray emission engine. Moreover, differences in the composition of X-ray emitting plasma may produce other differences: X-ray radiative losses, for example, are dominated by radiation of highly ionized atoms and therefore we may expect changes in the emission measure, as well as, in individual lines. Finally, if there was a difference in the disk fraction, we would expect an indirect effect on the global X-ray emission: Class II stars have lower X-ray luminosities than Class III stars (Stelzer & Neuhäuser, 2001; Flaccomio et al., 2003a; Stassun et al., 2004; Preibisch et al., 2005; Flaccomio et al., 2006; Telleschi et al., 2007) thus a different fraction of disked stars may affect the global X-ray luminosity function. The assumption of a universal X-ray luminosity function has been proposed by Feigelson & Getman (2005) and used to estimate the distance (Kuhn et al., 2010) and total populations of several young clusters (e.g. Getman et al., 2006; Broos et al., 2007). In this context, the study of a cluster lying in a very different environment could be helpful in demonstrating the universality of X-ray properties of young star forming regions and justify the use of X-ray luminosity functions to determine the properties of young clusters.

In order to investigate the X-ray properties of a cluster in the outer Galaxy and compare them to similar cluster in the inner regions of the Galaxy, we have identified, as a suitable target, the young ( $\sim 1\text{-}2$  Myr) cluster NGC 1893, whose galactocentric distance is 11 kpc (Prisinzano et al., 2011). NGC 1893 is in a spiral arm different than that of the Sun and it is located near the edge of the Galaxy, where the environmental condition are quite different from those of the solar neighborhood. Situated in the Aur OB2 association toward the Galactic anti-center, NGC 1893 is associated with the HII region IC 410 and the two pennant nebulae, Sim19 and Sim130 (Gaze & Shajn, 1952), known as “Tadpole”. It contains a group of early-type stars with some molecular clouds but only moderate extinction. Several studies (Vallenari et al., 1999; Marco & Negueruela, 2002; Sharma et al., 2007; Caramazza et al., 2008; Prisinzano et al., 2011) demonstrated that star formation is still ongoing and therefore we can study the X-ray properties of the PMS stars, with particular focus on the differences between the Class II and the Class III stars X-ray emission, given that the disk evolution may depend on the environment (Yasui et al., 2009). The morphology, the age distribution of the cluster and the star formation history have been studied in detail by Sanz-Forcada et al. (2011).

They find that the cluster has not relaxed yet to a spherical distribution, and it still has different episodes of stellar formation. The analysis of the age and disc frequency of the objects in NGC 1893, in relation with the massive stars and the nebulae, revealed an ongoing stellar formation close to the dark molecular cloud and the two smaller nebulae Sim 129 and Sim 130 (Sanz-Forcada et al., 2011). While both massive and low mass stars seem to form in the vicinity of the denser molecular cloud, Sim 130 and specially Sim 129 harbour the formation of low mass stars (Sanz-Forcada et al., 2011). A parameter that is still very uncertain for this cluster is the metallicity. As we discussed in Prisinzano et al. (2011), the literature studies about the metallicity of NGC 1893 have ambiguous results. In a paper focused on the Galactic metallicity, Rolleston et al. (2000) found for 8 NGC 1893 members a slight indication of under solar abundances, Daflon & Cunha (2004) show a marginal indication of subsolar metallicity for 2 members of the cluster, but these studies do not show a strong evidence of subsolar metallicity, therefore, as assumed also in Prisinzano et al. (2011), we adopt for NGC 1893 a solar metallicity.

This study is part of a large project aimed at investigating the star formation processes in the outer Galaxy and is based on a large observational campaign on the young cluster NGC 1893. The first results, concerning the joint Chandra-Spitzer large program “The Initial Mass Function in the Outer Galaxy: the star forming region NGC 1893” (P.I. G. Micela), have been presented in Caramazza et al. (2008). In that earlier work we have analyzed the *Spitzer* IRAC maps of NGC 1893 joined to the *Chandra* ACIS-I long exposure observation, giving the most complete census of the cluster to date. The IRAC observations of NGC 1893 allowed us to identify the members of the cluster with infrared excesses (Class 0/I and Class II stars), while the ACIS observation was used to select the Class III objects that have already lost their disks and have no prominent infrared excess. Although that first catalog of members was incomplete, the presence of 359 members indicates that NGC 1893 is quite rich, with intense star forming activity despite the “unfavorable” environmental conditions in the outer Milky Way. In Prisinzano et al. (2011), we continued the study of the properties of NGC 1893 by using deep optical and JHK data and compiling a catalog extending from X-rays to NIR data. In this second work, we have assessed the membership status of each star, finding 415 diskless candidate members plus 1061 young stellar objects with a circumstellar disk or Class II candidate members, 125 of which are also  $H_{\alpha}$  emitters. Moreover, optical and NIR photometric properties have been used to evaluate the cluster parameters. Using the diskless candidate members, the cluster distance has been found to be  $3.6 \pm 0.2$  kpc and the mean interstellar reddening  $E(B-V) = 0.6 \pm 0.1$  with evidence of differential reddening across the whole surveyed region. These previous studies show that NGC 1893 contains a conspicuous population of pre-main sequence stars with a disk fraction of about 70%, similar to that found in clusters of similar age in the solar neighborhood. This demonstrates that, despite the expected unfavorable conditions for star formation, very rich young clusters can form also in the outer regions of our Galaxy.

In the present work, as part of the same project, we present the in-depth analysis of 450 ks long *Chandra* ACIS-I observation, already introduced in Caramazza et al. (2008), focusing on the X-ray properties of the 1021 detected sources in light of the previous results of Caramazza et al. (2008) and Prisinzano et al. (2011). To put our work in context, we will compare the present study with the 850 ks long *Chandra* ACIS-I observation of the Orion Nebula Cluster (ONC), termed Chandra Orion Ultradeep

Project (COUP) (Getman et al., 2005). The COUP with 1616 detected sources provided one of the most comprehensive dataset so far acquired on the X-ray emission of PMSs. Several studies were conducted on the 1616 COUP detected sources, in order to characterize the X-ray emission and to understand the coronal processes in the PMS stars. For example, Preibisch et al. (2005) have analyzed the dependence of the X-ray luminosity on the stellar properties, finding for the Orion stars that  $L_X$  is a function of the mass, Wolk et al. (2005) have studied the variability of the solar mass stars, in order to have indication of the emission of the young Sun, (Favata et al., 2005) have investigated the geometry of flare loops, resulting in the first observational indications of magnetic structure connecting the star and the disk. These are just few of the several results of the COUP published in more than 20 papers. Since COUP gives the most comprehensive view of magnetic activity in young stars ever achieved in the nearest rich cluster of very young stars, it is used here as a touchstone for comparison with NGC 1893.

In the present paper, we analyse the properties of the X-ray sources in NGC1893, focusing, in particular, on the X-ray luminosity of low mass stars. We compare the X-ray properties of the NGC 1893 members with infrared excesses (hereafter Class II stars), as defined in Caramazza et al. (2008) and in Prisinzano et al. (2011) with the members without infrared excesses (hereafter Class III stars), that are classified as members of the cluster by means of their X-ray emission (see Caramazza et al., 2008; Prisinzano et al., 2011, for details). The outline of the present paper is the following: in §2 we describe the data reduction, the photon extraction procedure, and present our X-ray catalog. In §3 we describe the spectral analysis that we pursued by means of spectral fitting and quantile analysis of X-ray spectra. In §4 we compare the X-ray properties of Class II and Class III of NGC 1893 and in §5 we present the variability properties of the members. In §6 we discuss our results and in §7 we summarize our work.

## 2. Data Reduction

The X-ray observations of NGC 1893 combine four nearly consecutive exposures of the cluster taken in 2006 November and a fifth exposure taken in 2007 January for a total exposure time of  $\sim 440$  ks. The combined X-ray image is shown in Fig. 1. Source detection was performed by Caramazza et al. (2008) and we refer to that work for details of the observations and the detection method.

Starting from the Caramazza et al. (2008) catalog, we proceeded to the photon extraction of the source photons by means of ACIS EXTRACT<sup>1</sup> (AE) v3.131 (Broos et al., 2002), an IDL based package of tools that can assist the observer in performing the many tasks involved in analyzing a large number of point sources observed with the ACIS instrument on Chandra. AE makes extensive use of TARA<sup>2</sup>, a package of tools in the IDL language for visualizing and analyzing X-ray astronomical data in FITS format, CIAO (Fruscione et al., 2006)<sup>3</sup>, the data analysis system written for the needs of users of the Chandra X-ray Observatory, and FTOOLS<sup>4</sup>, a general package of software to manipulate FITS files.

The extraction of point sources performed with AE takes into account the Point Spread Function (PSF) for single sources,

which strongly depends on the off-axis distance ( $\theta$ ). While the PSF is narrow and approximately circular in the inner part of the field of view ( $\theta \lesssim 5'$ ), it has a non-Gaussian shape at large off-axis, becoming broader and more asymmetric.

Moreover AE calculates the shape of the model PSF at each source position (by means of the CIAO task MKPSF), considering also that the fraction of the PSF where photons are extracted depends on crowding. In this way, AE finds a compromise between having the largest PSF fraction (thus providing good photon statistics for further spectral and timing analysis) and having the best signal-to-noise ratio, not to mention the importance of avoiding the contamination from nearby sources.

After the calculation of the PSF shape, AE refines the initial source positions, in our case originally estimated by PWDetect (Damiani et al., 1997a) assuming a symmetric PSF, by correlating the source images with the model of local PSFs. Following AE science hints<sup>5</sup>, this last procedure was only used for those sources lying off-axis by greater than 5 arcmin (321 sources), while for the rest of the sources we simply adopt mean photon positions. Coordinates listed in Table 1, as well as their  $1\sigma$  uncertainties, are the result of this process.

After re-computing positions, AE defines source extraction regions as polygonal contours of the model PSF containing a specified fraction of source events ( $f_{\text{PSF}}$ ). Generally, we chose  $f_{\text{PSF}}=90\%$ , and computed the contours from the PSF for a mono-energetic source with  $E=1.49$  keV. For a few sources in the denser parts of the field of view this fraction was reduced so as to avoid contamination with other nearby sources, in the most extreme cases down to  $f_{\text{PSF}} \sim 40\%$ .

Although the ACIS-I instrumental background level is spatially quite uniform, the actual observed background varies substantially across the NGC 1893 field due to the extended PSF wings of bright sources and to their readout trails. Background was therefore estimated locally for each source, adopting once again the automated procedure implemented in AE, which defines background extraction regions as circular annuli with inner radii 1.1 times the maximum distance between the source and the 99% PSF contour, and outer radii defined so that the regions contains more than 100 “background” events. In order to exclude contamination of the regions by nearby sources, background events are defined from an image that excludes events within the inner annular radii of all the 1021 sources.

Results of the photon extraction procedure are listed in columns 7-10 of Table 1, where we give the background-corrected extracted source counts for 0.5-8.0 keV, the associated error and the total background counts expected. In summary, our 1021 X-ray sources span a wide range of photon flux, from  $\sim 3$  to  $\sim 7100$  photons during the exposure time. Most sources are faint (e.g. 60% have fewer than 50 photons).

In the last six columns of Table 1, we list some characteristics of the sources: the significance (signal-to-noise ratio), Kolmogorov-Smirnov probability that the lightcurves of the sources are constant, the median photon energy, the absorption-corrected X-ray luminosities and a flag indicating the method used to determine them.

## 3. Spectral Analysis

In order to determine the intrinsic luminosity of our sources, spectral analysis is necessary. Unfortunately, spectral fitting can be applied only to high counts sources while relatively faint

<sup>1</sup> [http://www.astro.psu.edu/xray/docs/TARA/ae\\_users\\_guide.html](http://www.astro.psu.edu/xray/docs/TARA/ae_users_guide.html)

<sup>2</sup> <http://www.astro.psu.edu/xray/docs/TARA/>

<sup>3</sup> <http://cxc.harvard.edu/ciao/index.html>

<sup>4</sup> <http://heasarc.gsfc.nasa.gov/docs/software/ftools/>

<sup>5</sup> [http://www.astro.psu.edu/xray/docs/TARA/ae\\_users\\_guide/node35](http://www.astro.psu.edu/xray/docs/TARA/ae_users_guide/node35)

11	052218.45+332820.8	80.576895	33.472458	0.1	6.6	311.8	19.0	30.2	0.9	15.9	0.128	359.1	1.4	31.13	a
12	052218.98+33250.6	80.579105	33.547401	0.4	7.9	34.6	10.0	51.4	0.89	3.3	0.661	348.2	2.7	30.28	c
13	052219.11+332421.4	80.579652	33.405964	0.3	7.5	62.3	11.8	59.7	0.89	5.0	0.199	348.4	2.0	30.8	b
14	052219.24+332259.2	80.580177	33.383129	0.4	8.3	85.2	13.1	65.8	0.9	6.2	0.038	345.9	2.9	30.97	b
15	052219.30+332904.9	80.580423	33.484722	0.3	6.4	41.0	8.9	28.0	0.9	4.3	0.0020	357.3	2.9	30.36	c
16	052219.53+332729.7	80.581412	33.458257	0.3	6.4	41.0	9.1	32.0	0.9	4.2	0.3	362.0	1.5	30.36	c
17	052219.52+332754.6	80.581338	33.465173	0.2	6.4	125.9	13.0	29.1	0.9	9.3	0.57	347.4	3.1	31.11	a
18	052219.66+333348.5	80.581954	33.563493	0.4	8.4	62.8	12.1	66.2	0.9	5.0	0.447	343.9	2.5	31.17	b
19	052219.97+332837.3	80.583228	33.477032	0.4	6.3	26.4	7.7	23.6	0.9	3.2	0.544	326.4	1.6	30.16	c
20	052220.26+332912.7	80.584438	33.486863	0.2	6.3	114.1	12.4	26.9	0.9	8.8	0.995	358.9	3.0	31.05	a
21	052220.39+332942.7	80.584974	33.495209	0.3	6.3	56.8	9.8	28.2	0.89	5.5	0.839	362.9	3.8	30.78	b
22	052220.47+332424.6	80.585307	33.406844	0.4	7.2	42.9	10.0	45.1	0.89	4.1	0.017	362.2	1.7	30.38	c
23	052220.46+332955.8	80.585257	33.498841	0.1	6.4	331.1	19.6	31.9	0.89	16.5	0.432	351.0	2.8	31.52	b
24	052220.62+333030.6	80.585958	33.50851	0.3	6.5	56.7	9.9	29.3	0.89	5.5	0.0090	346.4	1.6	30.16	b
25	052221.54+332851.2	80.589788	33.480892	0.1	6.0	294.7	18.4	23.3	0.9	15.6	0.0	368.3	1.6	31.44	a

*Note 1.* Table 1 is available in its entirety in the electronic edition.

Col. (1): X-ray catalog sequence number, sorted by RA.

Col. (2): IAU designation.

Cols. (3) and (4): Right ascension and declination for epoch J2000.0.

Col. (5): Estimated standard deviation of the random component of the position error,  $\sqrt{\sigma_x^2 + \sigma_y^2}$ . The single-axis position errors,  $\sigma_x$  and  $\sigma_y$ , are estimated from the single-axis standard deviations of the PSF inside the extraction region and the number of counts extracted.

Col. (6): Off-axis angle.

Cols. (7) and (8): Net counts extracted in the total energy band (0.5–8 keV) in the extraction region; average of the upper and lower  $1\sigma$  errors on col. (7).

Col. (9): Background counts expected in the source extraction region (total band).

Col. (10): Net counts extracted in the hard energy band (2–8 keV).

Col. (11): Fraction of the PSF (at 1.497 keV) enclosed within the extraction region. A reduced PSF fraction (significantly below 90%) may indicate that the source is in a crowded region.

Col. (12): Photometric significance computed as net counts divided by the upper error on net counts.

Col. (13): Kolmogorov-Smirnov probability that the lightcurves of the sources are constant.

Col. (14): Effective exposure time: approximate time the source would have to be observed on-axis (no telescope vignetting) on a nominal region of the detector (no dithering over insensitive regions of the detector) to obtain the reported number of counts.

Col. (15): Background-corrected median photon energy (total band).

Col. (16): Absorption-corrected X-ray luminosities.

Col. (17): Origin of the X-ray luminosity, in col. (15): (a) from fit to a one temperature model spectrum; (b) from analysis of quantiles; (c) from a conversion factor derived from the analysis of the quantiles.

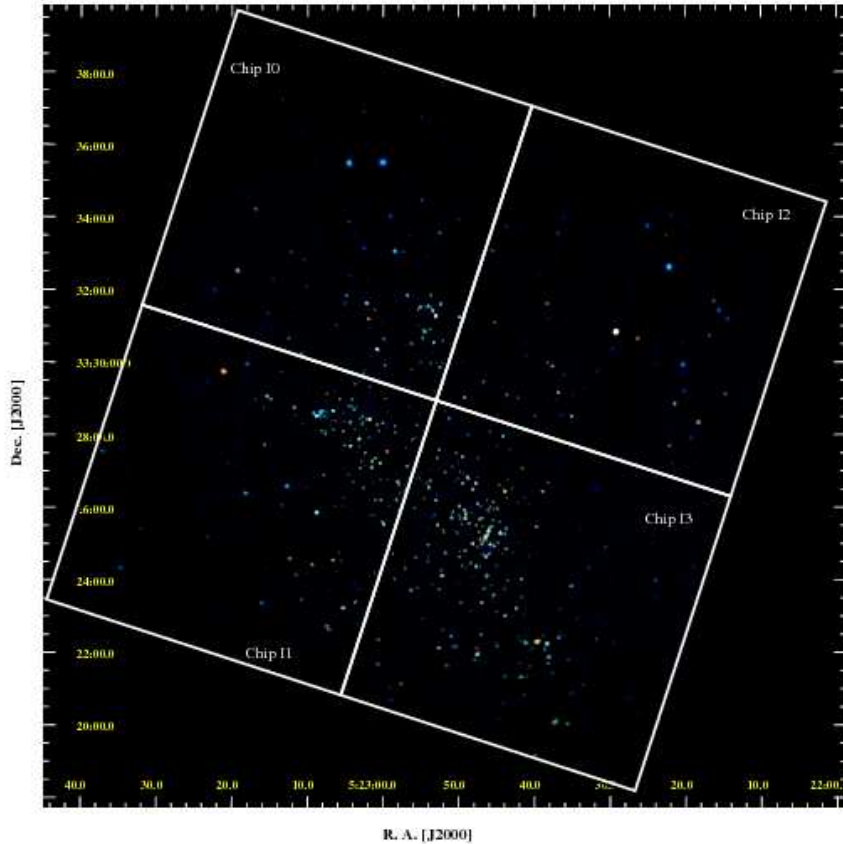


**Fig. 1.** True-color image of the young cluster NGC 1893. A kernel smoothing has been applied to highlight point sources. The energy bands of the RGB image are 0.5-1.1, 1.1-1.9, and 1.9-8.0 keV for red, green and blue colors. Brightness is scaled to the logarithm of the photon number in the displayed pixel. The color model depicts zero flux as black.

sources with poor statistics cannot be investigated using this method.

To overcome this limit, we decided to perform spectral fitting (§3.1) on 311 sources for which it is possible to bin the spectrum so that, in the background-subtracted (net) spectrum, each rebinned channel achieves a signal-to-noise ratio at least 3. In situations where the background level is high, this approach can produce higher quality binning compared to fixing a minimum number of counts in the source spectrum. For less intense sources we analyzed the spectrum of sources considering the quantiles of the distribution of energy for source counts. As we will describe in the following for sources down to 30 counts, applying a quantile method (Hong et al., 2004), we have been able to derive the values of  $N_H$  and  $kT$  interpolating directly from a thermal grid of models with a good accuracy, while for very low statistics sources we have used the quantile analysis to derive a median conversion factor from the count rate to the X-ray luminosity. Energy quantiles have been also used to discern the extragalactic contaminants.

### 3.1. Spectral Fitting

Reduced source and background spectra in the 0.5-8.0 keV band have been produced with AE (see §2), along with individual “redistribution matrices files” (RMF) and “ancillary response files” (ARF).

We fit our spectra assuming emission by a thermal plasma, in collisional ionization equilibrium, as modeled by the APEC code (Smith et al., 2001). Elemental abundances are not easily constrained with low-statistics spectra and were fixed at  $Z=0.3 Z_\odot$  (see Prisinzano et al., 2011), with solar abundance ratios taken from Anders & Grevesse (1989). The choice of sub-solar abundances is suggested by several X-ray studies of star forming regions (e.g. Feigelson et al., 2002; Maggio et al., 2007). Absorption was accounted for using the WABS model, parametrized by the hydrogen column density,  $N_H$  (Morrison & McCammon, 1983).

We fit source spectra with one-temperature (1T) plasma models using an automated procedure. In order to reduce the risk of finding a relative minimum in the  $\chi^2$  spaces, our procedure chooses the best fit among several obtained starting from a grid of initial values of the model parameters:  $\log(N_H) = 21.0, 22.0 \text{ cm}^{-2}$  and  $kT = 0.5, 1.0, 2.0, 10.0 \text{ keV}$ .

Among the 311 sources for which we conducted the spectral fitting, for 286 sources it was possible to determine  $N_H$  and  $kT$ . Using the spectral fit parameters, we have then derived X-ray luminosities for each of the 286 sources modeled with one-temperature spectrum, considering for NGC 1893 a distance of 3.6 kpc (Prisinzano et al., 2011). These sources are tagged with an “a” in column (16) in Table 1 and their luminosity is listed in column (15). The 25 sources for which we were unable to fit the spectra with a one temperature model, have been analysed with the study of the energy quantiles of the spectrum (see following sections).

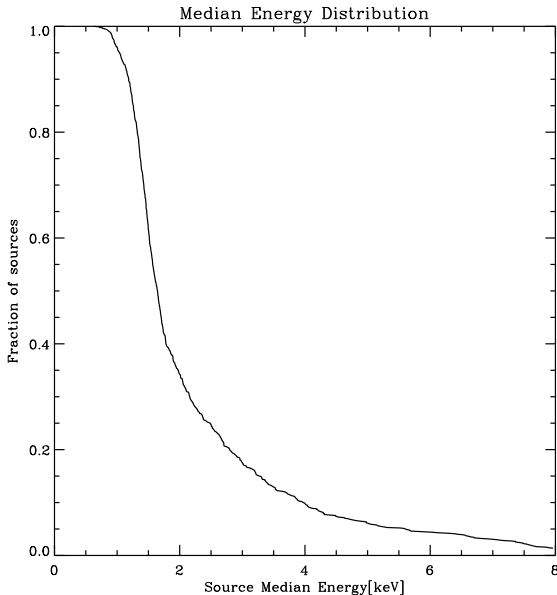


**Fig. 2.** Cumulative distribution function of the photon median energy of each source computed in the [0.5-8.0] keV range for all the sources.

### 3.2. Quantile Analysis

Spectral fitting analysis cannot be applied to faint sources, but a rough analysis of the whole sample can be achieved by the study of the median photon energy of each source. We plot in Fig. 2 the distribution of the source median energy computed in the [0.5-8.0] keV range. From this plot, we can retrieve some information about the population of our X-ray sources: the median value of the distribution is 1.6 keV, the bulk of the distribution is between 1 and 2 keV (62% of the median photon energy of the sources lies in this range), while 10% of the values are over 4 keV; this energetic tail of the distribution is probably due to extragalactic contaminants, even if we cannot exclude at this stage that stellar flares on NGC 1893 members play some role. While this kind of analysis is very helpful to understand the behavior of the entire sample, it does not help much for the characterization of single sources.

The conventional spectral classification of weak sources is often performed in the literature by means of the ratios of source counts in different spectral bands, i.e. X-ray hardness ratios (XHR) which can be considered “X-ray colors” (Schulz et al., 1989; Prestwich et al., 2003). The flaw in this method is that the choice of the bands is strongly related to the spectral shape and that, depending on the number of counts in each band, the error bar related to the ratio may be very large. For these reasons, we decide to apply an alternative method, introduced by Hong et al. (2004), that uses the energy value that divides photons into pre-determined fraction, instead of the ratio of counts in prefixed bands. Following Hong et al. (2004), if  $E_{x\%}$  is the energy below which the net counts are  $x\%$  of the total counts, quantile  $Q_x$  is  $Q_x = \frac{E_{x\%} - E_{lo}}{E_{up} - E_{lo}}$ , where  $E_{lo}$  and  $E_{up}$  are the lower and upper boundary of the full energy band, i.e. 0.5 and 8.0 keV in our case. The fractions we choose are the median (50% quantile), and the quartiles (25% and 75% quantiles). Since quantiles, for a given spectrum, are not independent, Hong et al. (2004) selected the independent variables  $\log(Q_{50}/(1 - Q_{50}))$  and  $3(Q_{25}/Q_{75})$ , in order to have information on the photon population in several portions of the spectrum. The derived quantile values will be compared

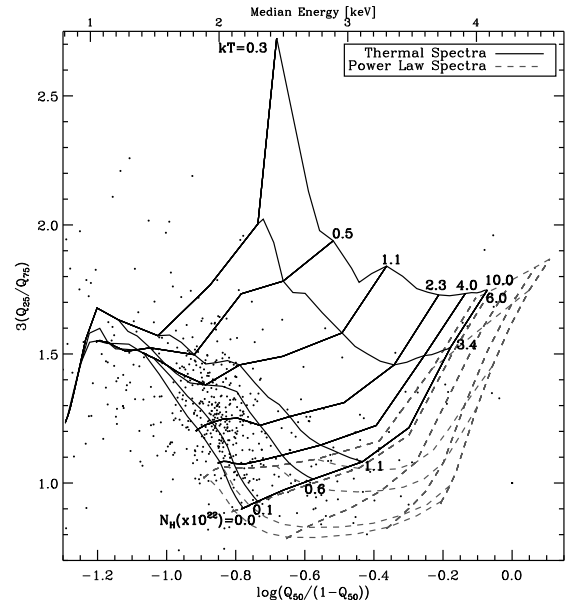


**Fig. 3.** Quantiles of X-ray spectra. The dots indicate the quantities derived from source energy quantiles. The two grids shows the same quantities derived from simulated spectra. The solid line grid refer to thermal spectra with  $N_H = [10^{20}, 10^{21}, 0.6 \cdot 10^{22}, 1.1 \cdot 10^{22}, 3.4 \cdot 10^{22}, 6 \cdot 10^{22}] \text{ cm}^{-2}$  and  $kT = [0.3, 0.5, 1.1, 2.3, 4.0, 10.0] \text{ keV}$ , while the dashed line grid to simulated power law spectra, typical of AGN, with the same  $N_H$  values and power law indices  $\Gamma = [0.0, 0.4, 1.0, 1.6, 2.0]$ .

with those calculated from simulated spectra in order to derive the best spectral parameters. Figure 3 shows the scatter plot of quantiles measured for our sources, compared with grids calculated from simulated spectra. The solid line grid refers to thermal spectra, while the dashed grid to power law spectra, with spectral index typical of AGNs (Brandt et al., 2001). We note that, as expected, most of the sources lies in the thermal grid region. By interpolating the loci of our sources inside the thermal grid it is possible to attribute values of  $N_H$  and  $kT$  to each source and derive the intrinsic X-ray luminosity at the distance of NGC 1893. In figure 4 we compare, for the brightest sources, the X-ray luminosity derived from the quantile analysis with that derived from spectral fitting. The luminosities derived spectral fitting are generally consistent with those derived from quantile analysis and a linear regression between the two luminosities results in a coefficient  $1.04 \pm 0.4$  giving strong support to the effectiveness of the method. The sources for which the luminosity was derived from the quantile analysis are indicated with a “b” in column (16) of table 1.

By analysing the sources outside the region covered by the thermal grid, we found three subclasses of objects:

- *Two temperatures spectra.* There is a small fraction of fairly strong sources (between 30 and 50 photons) that lie over the left bound of the thermal grid. Due to the concavity of the grid, this is the locus where thermal spectra characterized by two temperatures lie. For these cases, in our one temperature approximation, we associated them to the lowest  $N_H$  curve, interpolating just the  $kT$  value, that depends basically from the median energy of the spectrum (see Fig. 3).
- *Very poor statistics spectra.* Most of the sources outside the thermal grid are sources with less than 30 photons, with very large errors on quantiles. For these objects, we decided

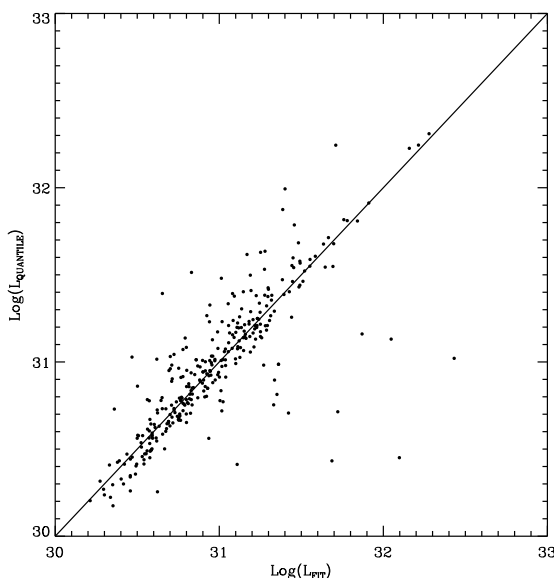


**Fig. 4.** Scatter plot of the X-ray luminosity derived from spectral fitting versus that derived from quantile analysis. The solid line indicates equal values of  $L_X$  derived with the two methods.

to adopt a single median conversion factor from count rate to luminosity. The conversion factor was derived from the quantile analysis of sources with more than 30 photons and applied to sources with less than 30 photons. These sources are indicated with a "c" in column (16) of Table 1.

– *Power law spectra*. A small fraction of the sources lie within the power law grid and will be discussed in §3.2.1.

### 3.2.1. Rejecting extragalactic contaminants

As shown above, with the energy quantiles analysis it is possible to attribute a luminosity to each source in the sample. It is also useful to investigate the contaminant population in the sample. NGC 1893 lies toward the galactic anticenter, therefore we expect to detect a large number of extragalactic sources. Moreover, the long exposure necessary to better investigate the faint population of our distant cluster results in a high probability of detecting AGNs. In order to estimate the number of AGNs, we considered the sensitivity for three different off axis regions in the *Chandra* ACIS-I field of view and calculated the minimum flux that we expect from a detected extragalactic source with a typical power law index  $\Gamma = 1.4$  (Brandt et al., 2001) in the direction of NGC 1893, ( $N_H = 6.56 \cdot 10^{21} \text{ cm}^{-2}$ , Dickey & Lockman, 1990). By comparing the obtained fluxes with the log N-Log S obtained from the Chandra Deep Field North (Bauer et al., 2004), we expect to find  $\sim 190$  AGNs among our sources.

From the diagram in Fig. 3, we find 128 sources that are outside the thermal grid and seem to be compatible with the power law grid. We have tagged them as candidate AGNs in our catalog, but we have not excluded them from further analysis. Caution is needed because a very hard spectrum, due e.g. to flares can be confused with a power law spectrum; indeed, from the analysis of the variability, we have found that 16 sources tagged as candidate AGN show big flares. The spectral analysis finds support from the spatial distribution of candidate AGNs. Looking at Fig. 1, the morphology of the cluster is evident and it is clear that the distribution of sources in the four instruments chips is not uniform. We compared the number of sources de-

tected in each chip with the number of candidate AGNs. As we expected, the total number of sources is higher in chips I1 and I3, where the peak density of the cluster lies, while the spatial distribution of the candidate AGNs is different and not related to the spatial distribution of the cluster. Again, we note that the candidate AGNs that show flares follow the same space distribution of the cluster, therefore we treat this population with caution but we do not exclude it from the sample. This analysis is summarized in Table 2.

### 3.3. Upper limit to the X-ray luminosity of undetected NGC 1893 members

The purpose of the present work is to examine the X-ray properties of the NGC 1893 members, investigate the properties of stars in different evolutionary stages and compare them with those of other star formation regions. For these reasons, we take advantage of the work described in Prisinzano et al. (2011) in which the optical and the infrared properties of NGC 1893 members are described. In order to compare the luminosity of stars from different classes without any bias due to different depth of infrared, X-ray and optical images, we derived upper limits to the X-ray luminosity for all the cluster members in Prisinzano et al. (2011) falling in the *Chandra* ACIS-I field of view and undetected in X-rays. Upper limits to the photon count rates were calculated with PWDetect (Damiani et al., 1997a,b), with a detection threshold significance set to  $4.6\sigma$ , the same used for source detection (Caramazza et al., 2008). In order to convert count rate upper limits into X-ray luminosity for X-ray undetected members, we calculated a conversion factor, considering the median value of the ratio between X-ray luminosity and count rate for the detected X-ray sources as done for the detected sources. In table 3 we list the sequence number of the source in Prisinzano et al. (2011), the coordinates and the upper limit to the X-ray luminosity of the 158 Class II members that we will analyse.

## 4. X-ray properties of low mass members

Focusing on the X-ray properties of the NGC 1893 low-mass members, we started from the member catalog of Prisinzano et al. (2011). In particular, we selected all the Class II or Class III candidate members with mass smaller than  $2 M_\odot$  and whose optical colors are compatible with the cluster locus. In order to have a complete sample of sources, we selected all the stars with mass greater than  $0.35 M_\odot$ , the choice of this completeness threshold derives from analysis of the color-magnitude diagram (fig. 11 in Prisinzano et al., 2011) and will be confirmed in the following. We also required that the candidate members are inside the *Chandra* ACIS-I field of view. In this way, we identify 591 low-mass members, 307 of which are Class II stars, while 284 are classified as Class III stars. Among the 591 members, 158 of the Class II stars are not detected in the X-ray observations, therefore we have only a determination of the upper limit to their X-ray luminosity. The following analysis is based on the sample of 591 low-mass members.

To compare the luminosity of different classes of objects, we analyzed the cumulative X-ray Luminosity Functions (XLF) of the Class II and Class III members. In order to take into account non-detections, XLFs were derived using the Kaplan-Meier maximum likelihood estimator (Kaplan & Meier, 1958). Figure 5 shows the comparison of the cumulative X-ray luminosity functions of Class II and Class III members. Looking at this global description, we note that the range of luminosity is  $3 \cdot 10^{29} - 3 \cdot 10^{31} \text{ erg s}^{-1}$ . It is evident that the Class III stars

**Table 2.** Number of detected X-ray sources and AGN candidates in the 4 *Chandra* ACIS-I chips.

CHIP	Number of X-ray Sources	Number of AGN Candidates
I0	158	28 (0 with flares)
I1	268	24 (5 with flares)
I2	143	30 (1 with flares)
I3	452	46 (10 with flares)

**Table 3.** Upper limit to the X-ray luminosities for NGC1893 X-ray undetected members

ID (Prisinzano et al., 2011)	$\alpha$ (J2000.0) (deg)	$\delta$ (J2000.0) (deg)	$\log L_{t,c}$ (ergs $s^{-1}$ )
(1)	(2)	(3)	(4)
408	80.562999	33.575532	30.47
316	80.566272	33.449992	30.31
454	80.580917	33.562509	30.56
123	80.580957	33.438989	30.22
57	80.590203	33.447045	30.29
213	80.598221	33.455573	30.08
492	80.598731	33.344828	30.42
342	80.602976	33.532386	30.24
497	80.603157	33.522741	30.26
458	80.606043	33.386557	30.27
508	80.613344	33.350895	30.35
134	80.617675	33.454839	30.11
319	80.618691	33.409851	30.09
533	80.620025	33.347069	30.61
439	80.620694	33.359367	30.32
164	80.624260	33.532496	30.06
146	80.624662	33.559724	30.16
267	80.626424	33.450228	29.91
445	80.628081	33.388558	30.16
334	80.637005	33.457892	30.09
418	80.637332	33.361037	30.26
93	80.640689	33.376491	30.17
553	80.641242	33.370493	30.2
452	80.641437	33.378881	30.15
422	80.642576	33.436029	29.9
546	80.644803	33.350252	30.67
243	80.647512	33.363512	30.71
459	80.648981	33.430316	29.9
469	80.650405	33.388107	30.06
522	80.660049	33.399277	30.01
575	80.662935	33.419157	29.85
390	80.663318	33.413863	29.88
348	80.663623	33.396689	30.02
394	80.671760	33.378814	30.28
337	80.676571	33.476855	29.7
466	80.677781	33.395425	30.01
506	80.679261	33.379202	30.12
136	80.680467	33.599258	30.31
496	80.680484	33.396474	30.1
544	80.681921	33.495006	29.7
296	80.684036	33.394367	30.18
501	80.684164	33.391812	30.05
381	80.684924	33.393304	30.02
524	80.689466	33.559017	30.39
168	80.689949	33.412581	30.16
476	80.690269	33.350649	30.23
472	80.691751	33.341261	30.28
456	80.692317	33.399608	30.15
480	80.693894	33.367976	30.13
54	80.697590	33.389405	31.02
320	80.697977	33.395933	29.94
434	80.698224	33.40569	31.37
488	80.699277	33.409286	29.88
362	80.701203	33.354283	30.21
165	80.702890	33.527785	30.29
513	80.703693	33.400595	29.95
389	80.704304	33.416291	29.82
427	80.706539	33.412613	29.85
289	80.707190	33.411752	29.86
94	80.707273	33.428734	30.37
413	80.707867	33.464616	29.68
504	80.708417	33.437063	29.71
401	80.709488	33.513873	29.89
437	80.710054	33.421240	30.37
364	80.710109	33.462006	29.71
447	80.710368	33.467710	29.64
195	80.711121	33.404267	29.91
449	80.711743	33.4208385	29.81
64	80.712482	33.567166	30.09
59	80.712499	33.388352	29.98

*Note 2.* Table 3 is available in its entirety in the electronic edition.

Col. (1): Prisinzano et al. (2011) sequence number, sorted by RA.

Col. (2) and (3): Right ascension and declination for epoch (J2000.0).

Col. (4): Estimated upper limit to the Absorption-corrected X-ray luminosities.

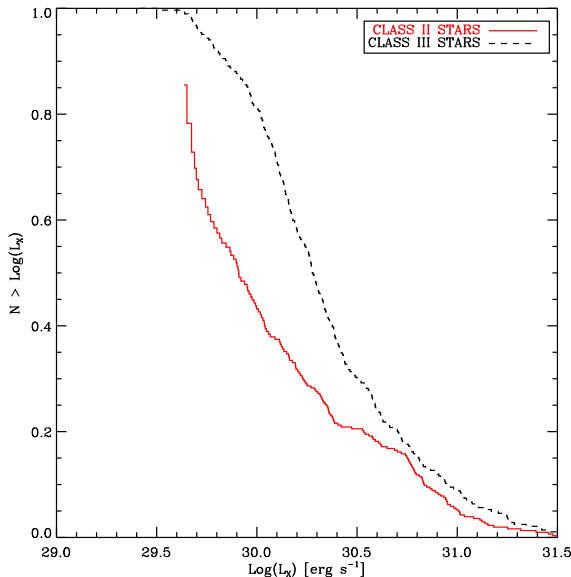


**Fig. 5.** Cumulative X-ray Luminosity Functions of the Class II and Class III members. The nondetections were taken onto account, deriving the XLFs with the Kaplan-Meier maximum likelihood estimator.

are brighter in X-rays, the median is higher and the body of the Class III object distribution is above that of Class II objects. At this age the dynamo mechanism is saturated in most of the PMS stars, therefore the X-ray luminosity scales as the bolometric luminosity of the star (e.g. Preibisch et al., 2005). This means that the difference in the whole XLF may be due to intrinsic properties or to a different bolometric luminosity (or mass) distribution among the two infrared classes. To avoid the mass dependence, it is usual to compare the XLFs in several ranges of mass (e.g. Flaccomio et al., 2003b; Preibisch et al., 2005; Prisinzano et al., 2008), despite the large errors caused by having few objects in each bin of mass. We overcome both of these difficulties by analysing the Class II and Class III X-ray luminosities as a function of the bolometric luminosity of the star. Figure 6 shows the quartiles (25%, 50%, 75%) of the  $L_X$  distribution in running intervals of bolometric luminosity covering 80 datapoints, for both of Class II (continuous line) and Class III (dashed line) stars. The resulting lines have been smoothed over scales of 0.1 in logarithm of bolometric luminosity. Note that for Class II stars the quartiles have been plotted only where the fraction of  $L_X$  upper limits does not affect the calculation of the quartiles themselves (e.g., the first quartile may be calculated only if  $L_X$  upper limits are less than 25%). The three quartiles give us different information about the distribution of  $L_X$ : the first quartile of Class III objects is similar to that correspondent to Class II stars, but we are able to calculate this value only for a small fraction of Class II member, due to the high fraction of  $L_X$  upper limits in the faint sample. The median and the third quartile, that describe the body and tail of the X-ray distributions respectively, show the same feature. They are lower for Class II members but the difference decreases with bolometric luminosity and for bright stars the quartiles are similar to those of Class III members.

In order to interpret these results, we also need to compare the value of  $L_X/L_{BOL}$  for the two infrared classes of objects. We show in Fig. 7 the three running quartiles of the distribution of  $L_X/L_{BOL}$  for Class II and Class III objects. We see that the ratio decreases for the two classes as a function of  $L_{BOL}$ . That

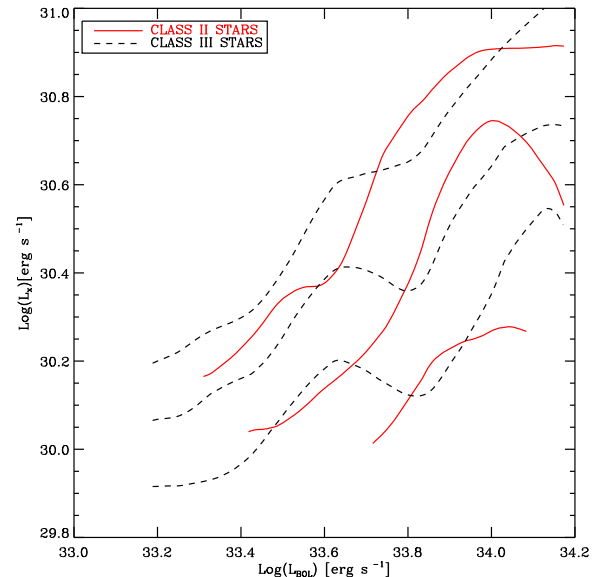


**Fig. 6.** X-ray luminosity distribution as a function of the stellar bolometric luminosity. The three couples of lines refer to the (25%, 50%, 75%) quartiles of the  $L_X$  distributions calculated in running intervals of  $L_{BOL}$  constituted by 80 contiguous points and smoothed in interval of bolometric luminosity of  $0.1 \text{ erg s}^{-1}$ . The continuous lines refer to Class II stars, while the dashed ones to Class III stars. The quartiles have been plotted just where the fraction of upper limit values does not affect the calculation of the quartile itself.

means that the fraction of stars in the saturated dynamo regime ( $L_X/L_{BOL} \sim 3$ ) decreases as a function of  $L_{BOL}$ , and the displacement of Class II  $L_X/L_{BOL}$  below that for Class III stars means that the fraction of unsaturated X-ray sources is larger for disked stars compared to diskless stars.

We also compared the global X-ray properties of the stars in NGC 1893 with those of the Orion Nebula Cluster, in particular those obtained from the Chandra Orion Ultradeep Project (COUP) (Getman et al., 2005). As we discussed in §1, COUP gives the most complete set of studies in X-rays for young stars ever achieved for such a rich cluster therefore it has been considered a touchstone and its results has been compared with previous and succeeding X-ray studies. Feigelson & Getman (2005) compared the COUP XLF with that of NGC1333 and IC 348 finding that "the shapes of different YSC XLFs appear to be remarkable similar to each other, once a richness-linked tail of high luminosity O stars is omitted". Also RCW38, IC1396N, NGC 6357, the Carina Nebula Cluster, M17 and NGC2244 (Wolk et al., 2006; Getman et al., 2007; Wang et al., 2007; Sanchawala et al., 2007; Broos et al., 2007; Wang et al., 2008) compared the X-ray properties of several clusters to COUP results, demonstrating that in the Sun neighbourhood the X-ray properties of star forming regions are similar, comparing clusters of similar age and accounting for the IMF. The only relevant difference in the XLF is for Cep OB3b (Getman et al., 2006), where the XLF has a different shape from that seen in the ONC with an excess at  $\text{Log}(L_X) \sim 29.7$  or  $0.3 M_\odot$ . The origin of the difference it is not clear but could be ascribable to a deviation in the IMF or some other cause, such as sequential star formation generating a non-coeval population.

Starting from these previous results, we consider the ONC as representative of the X-ray properties of nearby star forming

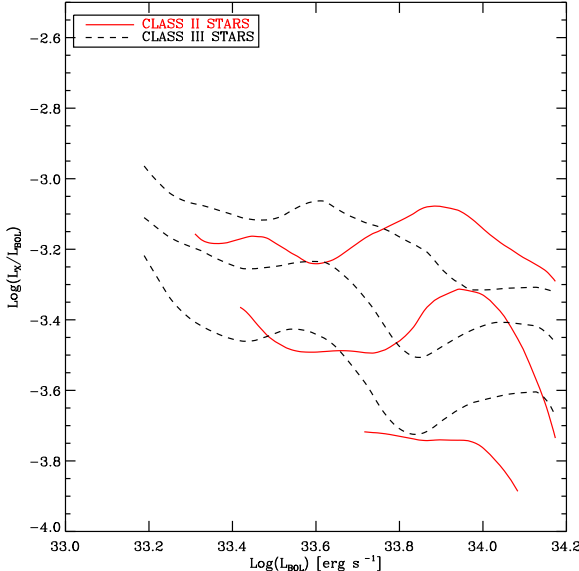


**Fig. 7.**  $L_X/L_{BOL}$  distribution as a function of  $L_{BOL}$ . The three couples of lines refer to the (25%, 50%, 75%) quartiles of the  $L_X/L_{BOL}$  distributions calculated in running intervals of constituted by 80 contiguous points and smoothed in interval of bolometric luminosity of  $0.1 \text{ erg s}^{-1}$ . The continuous line refer to Class II stars, while the dashed one to the Class III stars.

region and will compare COUP results with those of NGC 1893, that is  $\sim 10$  times more distant from the Sun. Figure 8 describes the quantiles of the  $L_X$  distributions for the Class II and Class III stars between  $0.35$  and  $2 M_\odot$  in the case of NGC 1893 (continuous line) and ONC (dotted line). The first quartile of the NGC 1893  $L_X$  distributions is similar to the ONC, and, since we know that the COUP sample is complete in this range of masses (Getman et al., 2005), it derives that our sample of stars has the same completeness of that of the ONC. The median of the two  $L_X$  distributions are similar, but we note that the third quartile is larger for the ONC at the faintest  $L_{BOL}$ . This means that we lack bright X-ray sources at the lowest masses in NGC 1893 and this cannot be related to an incompleteness of the sample: in that case we would loose faint stars and the effect would be enhanced. Albacete Colombo et al. (2007), comparing the X-ray properties of young stars in Cyg OB2 with those in the ONC, noted that dividing the COUP observation in 100 ks segments, a significant fraction of the longer and more energetic flares are missed. The difference between the two distributions could be therefore explained referring to the fact that COUP observation is longer than NGC 1893 ones, therefore in the ONC it is possible to observe rare very energetic flares that, even not modifying the median of the distribution, affect its tail. In order to take into account the effect of the duration of the observation, in the comparison of flares properties between NGC 1893 and the ONC (see §5), we will normalize for the exposure time.

## 5. X-ray Variability

We have analyzed the variability of the lightcurves of the X-ray sources, applying the Kolmogorov-Smirnov test to the arrival times of photons, and determined that 34% of our 1021 X-ray sources (including both members and non-members) are variable with a probability greater than 95%. If we restrict ourselves to only members, the variability fraction is 36 %. When split ac-

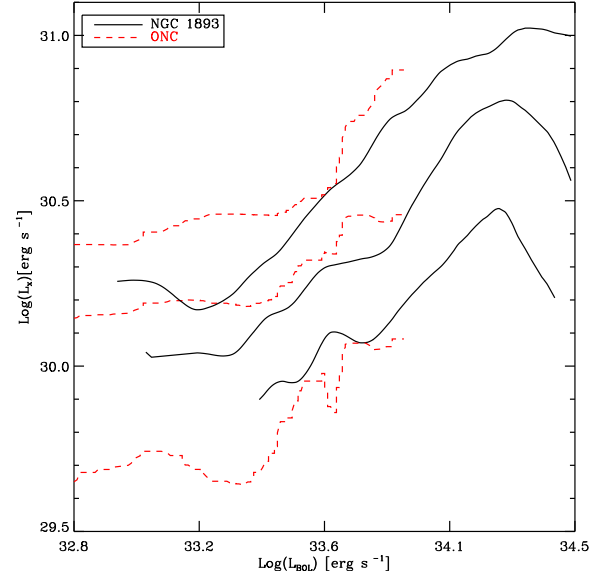


**Fig. 8.** X-ray luminosity distribution as a function of the bolometric luminosity. The three pairs of lines refer to the (25%, 50%, 75%) quartiles of the  $L_X$  distributions calculated in running intervals of bolometric luminosity constituted by 80 contiguous points and smoothed in intervals of bolometric luminosity of  $0.1 \text{ erg s}^{-1}$ . The continuous line refer to the NGC 1893 stars, while the dashed one to the ONC stars.

cording to whether a disk is present or not, 34% of the Class III stars are variable vs. 41 % of the Class II's. While we cannot state that these two numbers are statistically different, we have to take into account that Class II are intrinsically fainter than Class III stars and therefore the comparison has to be done analysing sources with the same statistics. Figure 9 shows the number of variable stars as a function of the minimum X-ray luminosity of the stars in the subsample. We note that, considering just the brightest stars, the discrepancy between Class II and Class III seems to be larger, suggesting a real difference in the fraction of variable stars in the two classes. It is interesting to investigate the behavior of Class II stars that still show accretion phenomena and those that do not present evidence of strong accretion. In the Prisinzano et al. (2011) catalog there is a subsample of Class II stars for which  $H_\alpha$  photometry is available. Using that tracer (see §5.3 in Prisinzano et al., 2011, for details on selection), we singled out 50 Class II X-ray emitters with ongoing accretion, as indicated by  $H_\alpha$  emission, and 77 that do not show strong  $H_\alpha$  emission. The two samples of Class II X-ray emitters show the same fraction of variable light curves.

A summary of the fraction of variable stars for the different subsamples of objects is given in Table 4.

The Kolmogorov-Smirnov test gives just a global indication of the variability of sources, but does not specify the nature of the variability. We therefore further analyzed the lightcurves in order to study the variability due to stellar flares. To single out flares in the lightcurves, we mapped the lightcurves using Maximum Likelihood Blocks (MLBs) (Wolk et al., 2005; Caramazza et al., 2007). The main characteristic of MLBs is that, being computed from the photon arrival times, their temporal length is not based on an *a priori* choice of temporal bin length, but depends on the light curve itself; for this reason MLBs are a useful tool to quantify different levels of emission, and in particular to detect short impulsive events, that might be missed by binning the

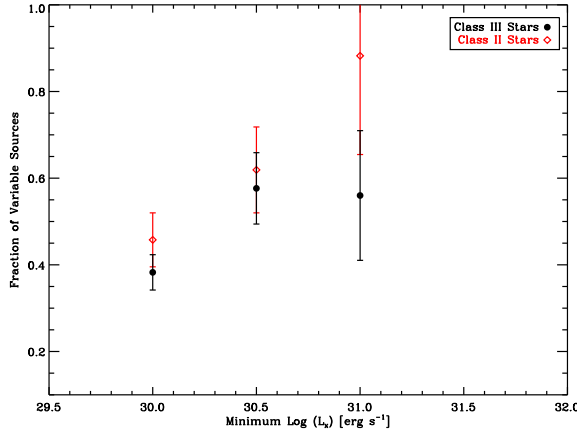


**Fig. 9.** Number of variable stars as a function of the minimum X-ray luminosity of the stars in the subsample. The vertical bars are the standard deviations ( $\sqrt{\text{Number of variable stars}}/\text{Number of stars in the subsample}$ ).

lightcurves using fixed length bins. Applying the same operational definition of flares described in Caramazza et al. (2007) that takes into account both the amplitude and time derivative of the count-rate, we singled out flares in the lightcurve as a sequence of blocks with a high count rate and a high rate of variation of the photon flux. We estimated the luminosity of each flare, scaling the total luminosity of the source during the observation by means of a count rate to luminosity conversion factor; we then computed the energy of each flare,  $E_{\text{flr}}$ , by multiplying the flare luminosity for the flare duration, calculated as the total temporal length of the blocks associated with the flare. The results of this analysis are summarized in Table 4, where we state the number of flares per source with energy larger than  $2 \cdot 10^{35}$  erg (this choice will be justified in the following).

In Fig. 10, we show the number of flares per source as a function of the minimum X-ray luminosity of the analysed subsample. Caramazza et al. (2007) demonstrated that the sensitivity of flare detection methods depends on source statistics, therefore it is interesting to compare the mean number of flares per source in several subsamples of sources, comprising sources with increasing luminosity. We note that for bright sources where we are able to detect all the flares, Class II stars are flaring significantly more than Class III stars and therefore that the disk plays an important role in generating this kind of high energy events.

According to the microflares hypothesis, originally proposed for the solar case (see Hudson, 1991), the X-ray emission of a star can be described as an ensemble of flares with a power law energy distribution:

$$\frac{dN}{dE_{\text{flr}}} = k \cdot E_{\text{flr}}^{-\alpha} \quad \text{with} \quad \alpha > 0 \quad (1)$$

where  $N$  is the number of flares with energies between  $E_{\text{flr}}$  and  $E_{\text{flr}} + dE_{\text{flr}}$ , emitted in a given time interval. If the index of the power law ( $\alpha$ ) is larger than 2 even very high levels of apparently quiescent coronal X-ray emission can be obtained from the integrated effects of many small flares. Figure 11 shows the cumulative distribution function (continuous line) of the intensity of flares for Class II and Class III members. For high counts the distribution is well described by a power law, but it progressively flattens towards low energies, likely because not all low-count flares are individually detectable.

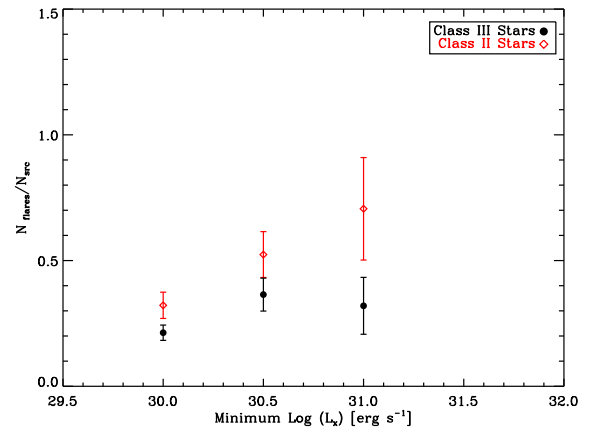


**Fig. 10.** Number of flare per source as a function of the minimum X-ray luminosity of the stars in the subsample. The vertical bars are the standard deviations as in Fig. 9.

Following the microflares hypothesis, we described the high energy part of the differential distribution of flare counts as a power law with index  $\alpha$ . The cumulative distribution is then described by a power law with index  $\alpha - 1$ .

We have determined the cutoff energy  $E_{\text{cut}}$  above which the observed distribution is compatible with a power law and the relative index  $\alpha - 1$ , with the same method used by Stelzer et al. (2006) (see also Crawford et al., 1970) :

$$\alpha - 1 = 1.2 \pm 0.2 \quad E_{\text{cut}} = 2 \cdot 10^{35} \text{ erg}$$

In agreement with our assumption on power law shape for the distribution, taking  $E_{\text{cut}}$  larger than the chosen cutoff, the best fit value of  $\alpha$  remains stable within the uncertainties, while under this threshold we cannot neglect the incompleteness effect.

Figure 11 also shows the cumulative distribution of flare energies for the Class II and Class III samples. We noticed that Class II star are more variable and more flaring than Class III objects, but we now see that the flares of Class II and Class III stars show the same distribution. We calculated the slope of the two power laws, finding for the two subsamples  $\alpha - 1 = 1.4 \pm 0.4$ .

Figure 12 shows the comparison between the cumulative distribution function of flare energies for NGC 1893 (solid line) and the ONC (dotted line). The distributions are normalized to the total number of sources of each sample and to the total exposure time. Above the completeness cutoff energy the two distributions are similar.

Figure 13 shows the comparison between the mean number of flares for the NGC 1893 and the ONC samples. In order to compare the same kind of flares, we considered only the flares over the completeness cutoff energy. We note that the number of flares per source is higher in the ONC but the difference decreases when we exclude low statistic sources. We infer that the difference may be due from a likely incompleteness of the NGC 1893 sample at low luminosities.

## 6. Discussion

The influence of the environment on star formation process may be investigated also through the analysis of X-ray emission. NGC 1893, for its position in the Milky Way is a good target to investigate possible differences in the behavior of stellar coronae and compare stars in clusters at the periphery of the Galaxy with those lying in dense spiral arms in the solar neighborhood.

**Table 4.** X-ray variability for different subsamples of X-ray sources

Sample	Number of sources	Fraction of variable sources (KS Test 95%)	Number of flares per source
All X-ray sources	1021	$0.34 \pm 0.02$	$0.16 \pm 0.02$
Class III X-ray sources	285	$0.34 \pm 0.03$	$0.19 \pm 0.02$
Class II X-ray sources	149	$0.41 \pm 0.05$	$0.27 \pm 0.04$
Accreting Class II X-ray sources	50	$0.40 \pm 0.09$	$0.30 \pm 0.08$
Not accreting Class II X-ray sources	77	$0.41 \pm 0.07$	$0.27 \pm 0.06$

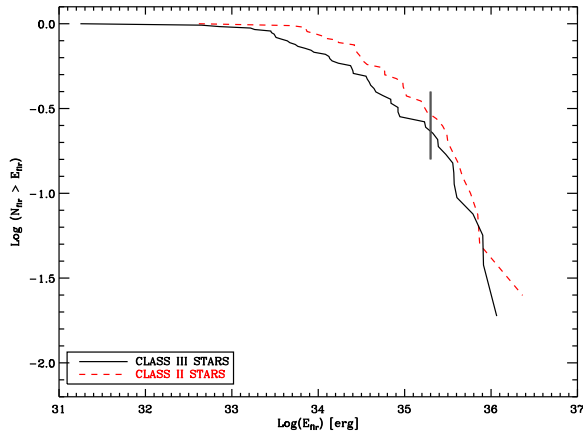


**Fig. 11.** Normalized cumulative distribution function of flare energies for Class III (solid line) and Class II stars (dashed line). In the range of energies above the cutoff value  $E_{cut} = 2 \cdot 10^{35}$  erg (vertical segment), the two distributions are compatible with a power law with  $\alpha - 1 = 1.4 \pm 0.4$ ; for low counts the distributions flatten, most likely because the detection of low-counts flares is incomplete.

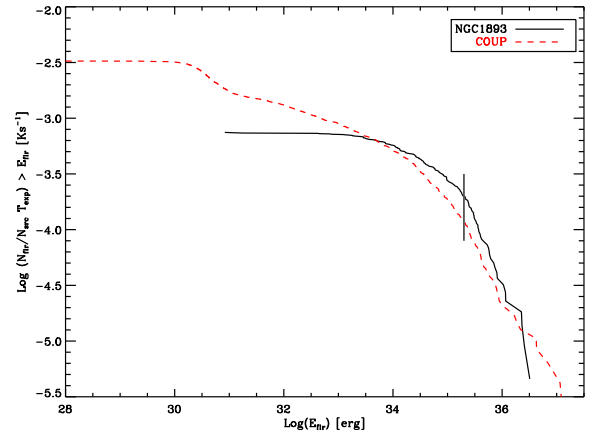


**Fig. 12.** Cumulative distribution function of flare energies for X-ray members in NGC 1893 (solid line) and ONC (dotted line). The distributions are normalized to the total number of sources of each sample and to the total exposure time. In the range of energies above the cutoff value  $E_{cut} = 2 \cdot 10^{35}$  erg (vertical segment), where both the flare energy distributions are complete, the distributions of the flares follow similar distributions.

We analyzed the X-ray properties of NGC 1893, in particular comparing the XLF of low mass ( $< 2M_{\odot}$ ) Class II and Class III young stellar objects. We confirmed the known result that the Classical T Tauri Stars (CTTS), i.e. the stars with signatures of disks, are globally less active than the Weak-lined T Tauri stars (WTTS), i.e. stars that have no signatures of optically thick disks (e.g. Preibisch et al., 2005), while being more variable. We further investigated this result, analysing the behavior of  $L_X$  as a function of the bolometric luminosity. The correlation between these variables is compatible with the well known saturated dynamo scenario, typical of pre-main sequence stars. Using the method described in §4, we demonstrated that, even considering stars with similar  $L_{BOL}$ , the median  $L_X$  is lower for Class II stars, even if the difference decreases for stars with high  $L_{BOL}$ . Our statistical analysis suggests that the fraction of unsaturated Class II members is larger than for the Class III members. This result is in agreement with the scenario in which accretors stars are less luminous than non-accreting stars (Stelzer & Neuhauser, 2001; Flaccomio et al., 2003a; Stassun et al., 2004; Preibisch et al., 2005; Flaccomio et al., 2006; Telleschi et al., 2007). However the reason why Class II should be underluminous in X-rays is

not well understood. There are four main ideas that have been formulated to explain the different behaviors of disked and diskless stars; two are related to the presence of disk itself and two to the presence of accretion from the disk: 1) The lower X-ray luminosity of Class II stars could be related to the higher extinction due to X-ray absorption by circumstellar disks, even if the COUP survey results do not support this idea (Preibisch et al., 2005). 2) A possible explanation is related to the magnetic braking: indeed there are examples of magnetic connection between the star and the disk leading to the idea that disked stars are on average slower than diskless stars (Favata et al., 2005; Rebull et al., 2006; Prisinzano et al., 2008) and have a weaker dynamo action with consequent lower X-ray emission. In this case, the dynamo process would be the same for the star with and without disk and the lower luminosity of CTTS could be attributed to the slower rotation of CTTS related to the presence of the disk. 3) The presence of accretion may alter the stellar structure and change the dynamo process itself (Preibisch et al., 2005), in this case the dynamo process could be different with different saturation limit for CTTS and WTTS. 4) Finally, Gregory et al. (2007) demonstrated that the corona is not able to heat all the

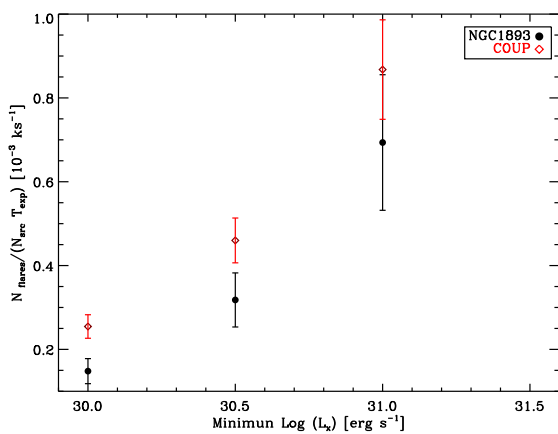


**Fig. 13.** Mean number of flares per kilosecond above the cutoff value  $E_{cut} = 2 \cdot 10^{35}$  erg for subsamples of X-ray sources with  $L_X$  larger than a given value. Circles refer to the NGC 1893 X-ray members, while diamonds to the ONC members. The vertical bars are the standard deviations as in Fig. 9.

material in the accretion columns and this cooler material, not visible in X-rays may obscure the line of sight to the star, reducing the X-ray emission. Recently, this scenario was also supported by Flaccomio et al. (2010) who found a correlation between the X-ray and optical variability for CTTS, while they did not find any correlation for WTTS. With our sample of data, we are not able to prefer one of the previous hypothesis, but we can add the observational constraint that the difference between the two classes of object is more evident for low mass stars and we can infer that this can be related to the different evolution time of disks around low mass stars and solar mass stars, causing there to be a larger fraction of disked stars at the lowest masses (Carpenter et al., 2006; Sicilia-Aguilar et al., 2006; Lada et al., 2006; Megeath et al., 2005).

We have also compared the X-ray properties of NGC 1893 with those of the ONC low mass members. At this age the dynamo mechanism is saturated for a large fraction of the stars and this leads to a dependence of  $L_X$  on the bolometric luminosity (e.g. Preibisch et al., 2005). Since we cannot *a priori* assume that the mass distribution in the two clusters is similar, we compared the two samples as a function of the bolometric luminosity. With this method, we obtained that the median of the two  $L_X$  distributions vs mass are similar, but the third quartile is larger for the ONC at the faintest  $L_{BOL}$ . This effect seems to indicate an intrinsic lack of bright X-ray sources at the lowest masses in NGC 1893. This difference with the ONC cannot be an indication of an incompleteness of the NGC 1893 sample because, in that case, we would lose faint stars and the effect would be in the opposite direction. This difference between the two clusters in the high luminosity tail of the  $L_X$  distributions could be ascribed to the longer duration of COUP observation: indeed, in the ONC there was the possibility to observe long energetic flares that enhance the third quartile of the distribution.

Analyzing the variability of Class II and Class III stars in our sample, we find the known results that Class II are more variable than Class III stars and show more flares. The explanation of this behavior can be related to the effect of accretion. Flaccomio et al. (2010) observed that the X-ray variability of disked stars can be due to the shielding of significant fraction of the coronal plasma by dense accretion streams of cold material (see Gregory et al., 2007). It is difficult to compare in detail the

variability of NGC 1893 sources with the Orion Nebula Cluster ones, because of the several biases due to the different distance and the different duration of the X-ray observations that lead to a different completeness of the samples. Taking into account these several biases we find that the X-ray flares in Orion and NGC 1893 show a similar energy distribution frequency, leading to indistinguishable behavior of the two clusters from the coronal variability point of view.

We conclude that despite its peculiar location in the Galaxy, NGC 1893 includes a rich population of Class II and Class III X-ray sources that have, both from the X-ray luminosity and X-ray variability point of view, similar properties to nearby star forming regions, such as the ONC. The fact that the X-ray properties of clusters in such different environments are so similar gives strong support to the Feigelson & Getman (2005) suggestion that the X-ray properties can be used as standard candles, providing a new instrument for measurement for distances of young clusters (Kuhn et al., 2010).

## 7. Summary and Conclusion

As part of the large multiwavelenght project *The Initial Mass Function in the Outer Galaxy: the star forming region NGC 1893*, we have analyzed the 450 ks Chandra Observations, and studied the X-ray properties of the 1021 detected sources. The X-ray data have been combined to optical, near and mid-infrared data (Prisinzano et al., 2011) in order to correlate the X-ray properties to the presence of disk and/or accretion. Below, we summarize the overall results of our investigations.

- We derived the X-ray luminosity for our 1021 sources taking advantage of spectral fitting for 311 X-ray bright stars and from quantile analysis of the other sources, finding a range of X-ray luminosity  $10^{29.5} - 10^{31.5}$  erg s<sup>-1</sup>. We have analyzed, in particular, the low mass stars X-ray luminosity taking into account the classification of candidate members in Class II and Class III members based on infrared excesses of Prisinzano et al. (2011). Class III stars appear intrinsically more X-ray luminous than Class II stars, even comparing stars with the same bolometric luminosity. This effect may be due to the presence of the "magnetically connected" disk itself or to the ongoing accretion from the disk to the star.
- We have evaluated the variability of X-ray lightcurve using the Kolmogorov-Smirnov test, finding that 34% of the sources appear to be variable. We have also searched for flares in our lightcurves finding 0.16 flares per source. We found that Class II stars are more variable and more flaring than Class III stars, while the flare energy properties are the same. This property may be related to the accreting cold material that obscures part of the X-ray emitting material, making accreting stars X-ray lightcurves more variable than the ones of diskless stars but also suggests that the presence of a disk plays a role in generating high energy events.
- Comparing the X-ray properties of NGC 1893 with those of the nearby star forming region ONC, we find that the X-ray properties in NGC 1893 are not affected by the environment and that a stellar population in the outer Galaxy may have the same coronal properties of nearby star forming regions. This provides a strong evidence of the universality of the X-ray properties, and, as a consequence, a useful tool to determine properties, such as the distance or the total population, of young clusters.

*Acknowledgements.* This research has made use of data obtained from the Chandra X-ray Observatory and software provided by the Chandra X-ray Center

(CXC) in the application packages CIAO, ChIPS, and Sherpa. We acknowledge financial contributions from ASI-INAF agreement I/009/10/0, from European Commission (contract N. MRTN-CT-2006-035890) and PRIN-INAF (P.I. Lanza). S.J.W. is supported by NASA contract NAS8-03060 (Chandra). We thank the referee for helpful suggestions and comments that improved this work.

## References

Albacete Colombo, J. F., Caramazza, M., Flaccomio, E., Micela, G., & Sciortino, S. 2007, *A&A*, 474, 495

Anders, E. & Grevesse, N. 1989, *Geochim. Cosmochim. Acta*, 53, 197

Bauer, F. E., Alexander, D. M., Brandt, W. N., et al. 2004, *AJ*, 128, 2048

Brandt, W. N., Alexander, D. M., Hornschemeier, A. E., et al. 2001, *AJ*, 122, 2810

Broos, P., Townsley, L., Getman, K., & Bauer, F. 2002, ACIS Extract, An ACIS Point Source Extraction Package, Pennsylvania State University

Broos, P. S., Feigelson, E. D., Townsley, L. K., et al. 2007, *ApJS*, 169, 353

Caramazza, M., Flaccomio, E., Micela, G., et al. 2007, *A&A*, 471, 645

Caramazza, M., Micela, G., Prisinzano, L., et al. 2008, *A&A*, 488, 211

Carpenter, J. M., Mamajek, E. E., Hillenbrand, L. A., & Meyer, M. R. 2006, *ApJ*, 651, L49

Crawford, D. F., Jauncey, D. L., & Murdoch, H. S. 1970, *ApJ*, 162, 405

Daflon, S. & Cunha, K. 2004, *ApJ*, 617, 1115

Damiani, F., Maggio, A., Micela, G., & Sciortino, S. 1997a, *ApJ*, 483, 350

Damiani, F., Maggio, A., Micela, G., & Sciortino, S. 1997b, *ApJ*, 483, 370

Dickey, J. M. & Lockman, F. J. 1990, *ARA&A*, 28, 215

Elmegreen, B. G. 1989, *ApJ*, 338, 178

Elmegreen, B. G. 2002, *ApJ*, 577, 206

Elmegreen, B. G. 2004, *Memorie della Societa Astronomica Italiana*, 75, 362

Ercolano, B. & Clarke, C. 2009, ArXiv e-prints

Favata, F., Flaccomio, E., Reale, F., et al. 2005, *ApJS*, 160, 469

Feigelson, E. D., Broos, P., Gaffney, J. A., et al. 2002, *ApJ*, 574, 258

Feigelson, E. D. & Getman, K. V. 2005, in *Astrophysics and space science library*, Vol. 154, The Initial Mass Function 50 Year Later, ed. E. Corbelli & F. Palla & H. Zinnecker (Dordrecht: Springer), 163–+

Fischer, D. A. & Valenti, J. 2005, *ApJ*, 622, 1102

Flaccomio, E., Damiani, F., Micela, G., et al. 2003a, *ApJ*, 582, 398

Flaccomio, E., Micela, G., Favata, F., & Alencar, S. P. H. 2010, *A&A*, 516, L8+

Flaccomio, E., Micela, G., & Sciortino, S. 2003b, *A&A*, 402, 277

Flaccomio, E., Micela, G., & Sciortino, S. 2006, *A&A*, 455, 903

Fruscione, A., McDowell, J. C., Allen, G. E., et al. 2006, in *Society of Photo-Optical Instrumentation Engineers (SPIE) Conference Series*, Vol. 6270, Society of Photo-Optical Instrumentation Engineers (SPIE) Conference Series

Gaze, V. F. & Shajn, G. A. 1952, *Izvestiya Ordona Trudovogo Krasnogo Znameni Krymskoj Astrofizicheskoy Observatorii*, 9, 52

Getman, K. V., Feigelson, E. D., Garmire, G., Broos, P., & Wang, J. 2007, *ApJ*, 654, 316

Getman, K. V., Feigelson, E. D., Townsley, L., et al. 2006, *ApJS*, 163, 306

Getman, K. V., Flaccomio, E., Broos, P. S., et al. 2005, *ApJS*, 160, 319

Gould, A., Flynn, C., & Bahcall, J. N. 1998, *ApJ*, 503, 798

Gregory, S. G., Wood, K., & Jardine, M. 2007, *MNRAS*, 379, L35

Hong, J., Schlegel, E. M., & Grindlay, J. E. 2004, *ApJ*, 614, 508

Hudson, H. S. 1991, *Sol. Phys.*, 133, 357

Kaplan, E. L. & Meier, P. 1958, *J. Amer. Statist. Assn.*, 457

Kuhn, M. A., Getman, K. V., Feigelson, E. D., et al. 2010, *ApJ*, 725, 2485

Lada, C. J., Muench, A. A., Luhman, K. L., et al. 2006, *AJ*, 131, 1574

Mac Low, M.-M. & Klessen, R. S. 2004, *Reviews of Modern Physics*, 76, 125

Maggio, A., Flaccomio, E., Favata, F., et al. 2007, *ApJ*, 660, 1462

Marco, A. & Negueruela, I. 2002, *A&A*, 393, 195

Mathis, J. S., Mezger, P. G., & Panagia, N. 1983, *A&A*, 128, 212

Megeath, S. T., Hartmann, L., Luhman, K. L., & Fazio, G. G. 2005, *ApJ*, 634, L113

Morrison, R. & McCammon, D. 1983, *ApJ*, 270, 119

Padoa, P. & Nordlund, . 1999, *ApJ*, 526, 279

Pizzolato, N., Ventura, P., D'Antona, F., et al. 2001, *A&A*, 373, 597

Preibisch, T., Kim, Y., Favata, F., et al. 2005, *ApJS*, 160, 401

Prestwich, A. H., Irwin, J. A., Kilgard, R. E., et al. 2003, *ApJ*, 595, 719

Prisinzano, L., Micela, G., Flaccomio, E., et al. 2008, *ApJ*, 677, 401

Prisinzano, L., Sanz-Forcada, J., Micela, G., et al. 2011, *A&A*, 527, A77+

Rebull, L. M., Stauffer, J. R., Megeath, S. T., Hora, J. L., & Hartmann, L. 2006, *ApJ*, 646, 297

Reylé, C. & Robin, A. C. 2001, *A&A*, 373, 886

Rolleston, W. R. J., Smartt, S. J., Dufton, P. L., & Ryans, R. S. I. 2000, *A&A*, 363, 537

Sanchawala, K., Chen, W.-P., Lee, H.-T., et al. 2007, *ApJ*, 656, 462

Santos, N. C., Israelian, G., & Mayor, M. 2003, in *The Future of Cool-Star Astrophysics: 12th Cambridge Workshop on Cool Stars, Stellar Systems, and the Sun* (2001 July 30 - August 3), eds. A. Brown, G.M. Harper, and T.R. Ayres, (University of Colorado), 2003, p. 148-157., ed. A. Brown, G. M. Harper, & T. R. Ayres, Vol. 12, 148–157

Sanz-Forcada, J., Prisinzano, L., Micela, G., Caramazza, M., & Sciortino, S. 2011, submitted

Schulz, N. S., Hasinger, G., & Truemper, J. 1989, *A&A*, 225, 48

Sharma, S., Pandey, A. K., Ojha, D. K., et al. 2007, *MNRAS*, 380, 1141

Shu, F. H., Adams, F. C., & Lizano, S. 1987, *ARA&A*, 25, 23

Sicilia-Aguilar, A., Hartmann, L., Calvet, N., et al. 2006, *ApJ*, 638, 897

Smith, R. K., Brickhouse, N. S., Liedahl, D. A., & Raymond, J. C. 2001, *ApJ*, 556, L91

Snell, R. L., Carpenter, J. M., & Heyer, M. H. 2002, *ApJ*, 578, 229

Stassun, K. G., Ardila, D. R., Barsony, M., Basri, G., & Mathieu, R. D. 2004, *AJ*, 127, 3537

Stelzer, B., Flaccomio, E., Briggs, K., et al. 2006, ArXiv Astrophysics e-prints

Stelzer, B. & Neuhäuser, R. 2001, *A&A*, 377, 538

Telleschi, A., Güdel, M., Briggs, K. R., Audard, M., & Palla, F. 2007, *A&A*, 468, 425

Vallenari, A., Richichi, A., Carraro, G., & Girardi, L. 1999, *A&A*, 349, 825

Wang, J., Townsley, L. K., Feigelson, E. D., et al. 2008, *ApJ*, 675, 464

Wang, J., Townsley, L. K., Feigelson, E. D., et al. 2007, *ApJS*, 168, 100

Wilson, T. L. & Matteucci, F. 1992, *A&A Rev.*, 4, 1

Wolk, S. J., Harnden, F. R., Flaccomio, E., et al. 2005, *ApJS*, 160, 423

Wolk, S. J., Spitzbart, B. D., Bourke, T. L., & Alves, J. 2006, *AJ*, 132, 1100

Wouterloot, J. G. A., Brand, J., Burton, W. B., & Kwee, K. K. 1990, *A&A*, 230, 21

Yasui, C., Kobayashi, N., Tokunaga, A. T., Saito, M., & Tokoku, C. 2009, *ApJ*, 705, 54